

FIMP Dark Matter in bulk viscous non-standard cosmologies

Esteban González,^{1,*} Carlos Maldonado,^{2,†} N. Stefanía Mite,^{1,‡} and Rodrigo Salinas^{1,§}

¹*Departamento de Física, Universidad Católica del Norte,
Avenida Angamos 0610, Casilla 1280, Antofagasta, Chile*

²*Facultad de Medicina y Ciencia, Universidad San Sebastián,
Lago Panguipulli 1390, 5501842, Puerto Montt, Chile*

In this paper, we revisited the extension of the classical non-standard cosmological model in which dissipative processes are considered through a bulk viscous term in the new field ϕ , which interacts with the radiation component during the early universe. Specifically, we consider an interaction term of the form $\Gamma_\phi \rho_\phi$, where Γ_ϕ represents the decay rate of the field and ρ_ϕ denotes its energy density, and a bulk viscosity described by $\xi = \xi_0 \rho_\phi^{1/2}$, within the framework of Eckart's theory. This extended non-standard cosmology is employed to examine the parameter space for the production of Feebly Interacting Massive Particles (FIMPs) as Dark Matter candidates. In particular, for certain combinations of the model and Dark Matter parameters, namely (T_{end}, κ) and $(m_\chi, \langle \sigma v \rangle)$, we found large new regions in which it can establish the Dark Matter and reproduce the current observable relic density as compared with the Λ CDM and the classical non-standard cosmological scenarios.

Keywords: non-standard cosmologies, dissipative cosmologies, FIMP dark matter candidates, particle physics and cosmology connection.

I. INTRODUCTION

The Λ CDM model is currently the most successful cosmological framework for describing the evolution of the universe and fitting observational cosmological data. This model aligns well with various cosmological observations, including type Ia supernovae [1–3], measurements of the Hubble parameter [4–6], baryon acoustic oscillations [7], the cosmic microwave background [8, 9], among others. Regardless of its success, the model faces significant challenges, particularly concerning the nature of Dark Matter (DM) and Dark Energy (DE), where the first one, an as-yet-undetermined non-baryonic component of the universe, is estimated to be approximately five times more abundant than ordinary matter [9]. In this contexts, various theoretical frameworks, such as Supersymmetry [10] and string theory [11], suggest potential DM candidates. These are generally classified into three primary categories: Weakly Interacting Slim Particles (WISPs) [12, 13], Weakly Interacting Massive Particles (WIMPs) [14–18], and Feebly Interacting Massive Particles (FIMPs) [19–21]. The first category is composed of light particles that are produced via non-thermal mechanisms to prevent them becoming relativistic. Representative particles in this category include Axions, Axion-like particles, and Hidden Photons (or Dark Photons). In contrast, WIMPs are generated in thermal equilibrium with the Standard Model (SM) bath. With the ongoing expansion of the universe, WIMPs cease to be in thermal equilibrium through a process known as Freeze-Out, as their interaction rates become increasingly inefficient

relative to the expansion rate of the universe. These particles gained significant attention due to the so-called WIMP Miracle, which means that they can account for the observed DM relic density by assuming an interaction cross-section near the Electroweak scale and a particle mass around 100 GeV. To be consistent with observations within the Λ CDM framework, the total thermally averaged annihilation cross-section for this category must be approximately $\langle \sigma v \rangle_0 = \text{few} \times 10^{-9}$ GeV [22]. However, the entire parameter space for WIMPs has been extensively explored, with no positive detection signals to date. In this direction, FIMPs emerge as candidates that are produced through non-thermal mechanisms and never achieve thermal equilibrium with the surrounding medium. Consequently, these particles undergo a process known as Freeze-In to establish their population. To prevent FIMPs from reaching equilibrium, their interaction strengths must be weaker than those of WIMPs, rendering FIMPs highly elusive. Their feeble interactions make it challenging to detect them with current experimental instruments. Therefore, it is crucial to explore new DM candidates, production mechanisms, or alternative cosmological scenarios.

In the Λ CDM framework, it is assumed that DM sets its abundance during an era dominated by radiation, which dictates the parameters used in its search. Interestingly, the introduction of an additional field (ϕ) into the early universe can modify its expansion rate and lead to the so called non-standard cosmological histories. Such modifications may result in the DM relic density being set during epochs other than the radiation-dominated period, affecting its final abundance. When the field decays into SM particles, it results in an injection of entropy into the SM bath, thereby expanding the parameter space available for detecting these DM particles [23–50]. Similarly, non-standard cosmological models, such as bi-metric model, can also lead to non-standard histo-

* esteban.gonzalez@ucn.cl

† carlos.maldonado@uss.cl

‡ nelly.mite@ucn.cl

§ rodrigo.salinas@alumnos.ucn.cl

ries by generating entropy injections into the SM bath [51], which can affect DM production [52, 53]. These alternative scenarios, known as Non-Standard Cosmologies (NSCs), offer new avenues for DM detection and may reopen parameter spaces previously excluded in the Λ CDM model, potentially revealing viable DM candidates and mechanisms within these non-standard frameworks.

If DM is experimentally detected, then its particle physics properties and characteristics, such as mass, interactions with SM particles, and coupling constants, must be determinate. Nevertheless, understanding the production mechanisms of the DM candidate and the process that determines its abundance is critical for accurately assessing its current relic density. In this regard, if the interaction properties of the detected DM match the predicted annihilation cross-section $\langle\sigma v\rangle_0$, then it would support the Λ CDM model. Otherwise, if the interactions deviate from these expectations, it becomes necessary to consider alternative cosmological models that may more accurately explain the observed relic density of DM. One approach to developing new NSC models is to introduce non-perfect fluids into the early universe.

In cosmology, the matter components of the universe are typically modeled as perfect fluids, offering a robust approximation of the cosmic medium. However, perfect fluids are described by the thermodynamic in equilibrium, where their entropy remains constant, with a dynamic fully reversible. When non-perfect fluids are taken into account, phenomena like viscosity arise, offering a more precise and realistic depiction of cosmic fluids [54]. These effects play a crucial role in many cosmological processes, including the reheating of the universe, the decoupling of neutrinos from the cosmic plasma, nucleosynthesis, and others. Moreover, viscosity is significant in various astrophysical mechanisms, such as the collapse of radiating stars into neutron stars or black holes, and the accretion of matter around compact objects [54]. In this context, the behavior of viscous fluids must be described through relativistic thermodynamic frameworks for non-perfect fluids, such as Eckart's [55, 56] or Israel-Stewart formalism [57, 58]. Although Eckart's theory is non-causal [59], it remains widely studied due to its mathematical simplicity compared to the non-truncated Israel-Stewart theory. Nevertheless, Eckart's formalism serves as a convenient starting point for understanding dissipative effects in the universe, since Israel-Stewart theory reduces to Eckart's theory when the relaxation time for transient viscous effects is negligible [60].

In hydrodynamics, it is well established that viscosity manifests in two forms: shear and bulk viscosity. While shear viscosity can play a significant role in certain contexts [61], our focus will be on bulk viscosity, which can emerge due to the presence of mixtures in the universe. In this sense, in a single-fluid description, the universe as a whole can be characterized by the particle number density, n , according to the expression $n = n_1 + \dots + n_i$. Therefore, the simple assumption of different cooling rates in the expanding mixture can lead

to a non-vanishing viscous pressure [62]. On the other hand, bulk viscosity may also arise from DM decaying into relativistic particles, which naturally produce dissipative effects in the cosmic fluid [63, 64]. Furthermore, bulk viscosity can also emerge in the Cold Dark Matter (CDM) fluid due to the energy transfer between CDM and the radiation fluid [65]. Last but not least, bulk viscosity might exist in a hidden sector, reproducing various observational properties of disk galaxies [66, 67]. From the point of view of cosmological perturbations, viscous fluid dynamics has been shown to provide a simple and accurate framework for extending the description of cosmological perturbations into the nonlinear regime [68]. The recent advancements in gravitational wave detection have further opened up the possibility of observing dissipative effects in DM and DE through the dispersion and dissipation experienced by these waves as they propagate through a non-perfect fluid [69]. Additionally, bulk viscosity could contribute significantly to the emission of gravitational waves during neutron star mergers [70].

Bulk viscous effects in the matter components of the universe has been deeply and widely studied in the literature, particularly about viscous DE components [71–76]. However, a more common approach is to study a DM component that undergoes dissipative processes during its cosmic evolution [77–84]. This approach is of particular interest because it can account for the recent accelerated expansion of the universe without requiring an explicit DE component, leading to unified DM models [85–95]. Previous studies have explored dissipative stiff matter fluids within the framework of the full Israel-Stewart theory [96]. Furthermore, bulk viscous DM has been analysed in various contexts, including inflation [60, 97–99], interacting fluids [62, 100, 101], and modified gravity [75, 102]. These effects have also been studied concerning singularities such as the Big Rip and Little Rip, across both classical and quantum regimes [71, 73, 75, 103–110]. Further research has investigated the role of bulk viscosity in the radial oscillations of relativistic stars as well as its cosmological implications for Quark-Gluon plasma-filled universes [111, 112]. Finally, bulk viscosity has also been proposed as an alternative to mitigate some of the recent tensions in the Λ CDM model. For instance, a decaying DM scenario increases the expansion rate relative to Λ CDM, potentially alleviating the H_0 and σ_8 tensions [113]. Also, viscosity has been explored as a viable solution for the H_0 tension in Refs. [114–116] (for a comprehensive review of viscous cosmology in the early and late universe, see Ref. [117]).

In Ref. [118] the authors propose a novel NSC scenario in which the early universe is dominated by two interacting fluids, namely the new field ϕ and radiation, by considering that ϕ experiences dissipative processes during their cosmic evolution in the form of a bulk viscosity. Working in the framework of Eckart's theory for non-perfect fluids, the authors consider an interaction term of the form $\Gamma_\phi\rho_\phi$, where Γ_ϕ represents the decay rate of the field and ρ_ϕ denotes its energy density, and a bulk

viscosity described by $\xi = \xi_0 \rho_\phi^{1/2}$. The latter has the advantage that, when the field fully decays, the dissipation is negligible and the standard Λ CDM cosmology is fully recovered. This novel NSC scenario was applied to the study of the parameter space for WIMP DM candidates production, showing that it is possible to explore even wider regions in which the model can account for the actual DM relic abundance in the universe. This result is obtained by comparing the classical NSC scenario with their bulk viscous counterpart, considering same values for the NSC parameters, namely, κ , T_{end} , ξ_0 , and ω ; and for the WIMP DM candidate, namely m_χ and $\langle\sigma v\rangle$ (we define these parameter latter through the text). From the study, it can be noted that in the bulk viscous NSC there is a boost in the production of the field ϕ in comparison with the NSC case, and, therefore, an increased injection of entropy to the SM bath. On the other hand, for certain values of the parameter space (T_{end}, κ), it can be observed that the model with viscosity allows a considerable range of lower values of κ to reproduce the DM relic density compared with the NSC. The latter means that for larger values of κ both cases, NSC with and without bulk viscosity are comparable due to the contribution of the viscosity being almost neglected, and the addition of viscosity enables a bit larger values of T_{end} . Also, in the $(m_\chi, \langle\sigma v\rangle)$ space for the WIMP DM candidate in the same range of masses, NSC and NSC with bulk viscosity allow higher values of m_χ unlike the Λ CDM model, and the effects of dissipative processes let us to explore smaller total thermal averaged annihilation cross-section for the candidate. These results raise the following question: How do dissipative processes influence the parameter space for DM genesis in other DM candidates, such as FIMPs?

The aim of this paper is to revisit the bulk viscous non-standard cosmology studied in [118] by investigate the impact of this dissipative effects on the production and relic density of FIMP DM candidates. Following the same scheme as in [118] for WIMP DM candidates, we investigate the parameter space that can accurately reproduce the current DM relic density by adjusting both the model and DM parameters within this novel NSC framework for FIMP DM candidates.

This paper is organized as follows: Section II provides a brief review of the original NSC scenario. Subsection II A examines its applicability to FIMP DM candidates. In section III, we introduce the bulk viscous extension to the original NSC model, and compare the two models in subsection III A. The analysis of the parameter space for DM production that results in the current relic density is presented in Subsection III B. Finally, in Section IV, we present some conclusions and future directions. Throughout this paper, we use $c = 1$ units.

II. NON-STANDARD COSMOLOGIES

In the Λ CDM model, the total energy density of the early universe consists of radiation (ρ_γ) and DM (ρ_χ), with the contribution from the cosmological constant being insignificant compared to these components. As discussed in Refs. [23, 30–36, 38–40, 43, 44, 49], a direct approach to generating NSC scenarios involves introducing an additional field, ϕ , in the early universe, with an associated energy density, ρ_ϕ , which decays into SM plasma. The Friedman and the continuity equations in this scenario are

$$3H^2 = \frac{\rho_t}{M_p^2}, \quad (1)$$

$$\dot{\rho}_t + 3H(\rho_t + p_t) = 0, \quad (2)$$

where “dot” denotes the derivative with respect to the cosmic time, $H \equiv \dot{a}/a$ is the Hubble parameter, with a representing the scale factor, and $M_p = 2.48 \times 10^{18}$ GeV refers to the reduced Planck mass. The total energy density and pressure of the universe are $\rho_t = \rho_\gamma + \rho_\phi + \rho_\chi$ and $p_t = p_\gamma + p_\phi + p_\chi$, respectively. Additionally, in both the Λ CDM and NSC scenarios, the DM component is governed by the following Boltzmann equation, which describes its number density n_χ

$$\dot{n}_\chi + 3Hn_\chi = -\langle\sigma v\rangle (n_\chi^2 - n_{\text{eq}}^2), \quad (3)$$

where $\langle\sigma v\rangle$ is the total thermal averaged annihilation cross-section and n_{eq} is the equilibrium number density defined as $n_{\text{eq}} = m_\chi^2 T K_2(m_\chi/T)/\pi^2$, with K_2 the Bessel function of second kind, m_χ the DM mass and T the temperature of the universe. The DM energy density is related to its mass by $\rho_\chi = m_\chi n_\chi$.

To take into consideration the relativistic degrees of freedom, it is necessary to incorporate in the system the entropy density (s) of the universe, which is defined in terms of the radiation energy density as follows:

$$s = \frac{\rho_\gamma + p_\gamma}{T} = \frac{2\pi^2}{45} g_{\ast s}(T) T^3, \quad (4)$$

where $g_{\ast s}(T)$ are the degrees of freedom contributing to the entropy density. Hence, by assuming an interaction between the new field ϕ and the radiation component, we can obtain from Eqs. (2) and (4) the equations

$$\dot{s} + 3Hs = \frac{\Gamma_\phi \rho_\phi}{T}, \quad (5)$$

$$\dot{\rho}_\phi + 3(\omega + 1)H\rho_\phi = -\Gamma_\phi \rho_\phi. \quad (6)$$

In the latter, we assume a barotropic equation of state (EoS) for the field, expressed as $p_\phi = \omega\rho_\phi$, where ω is known as barotropic index. In these equations, $\Gamma_\phi \rho_\phi$ is the interaction term, with Γ_ϕ representing the decay rate of the new field. This interaction constitutes the simplest and most extensively studied case in NSC scenarios. It is important to note that the energy density for the DM candidate can be decoupled from the system due to its

negligible contribution compared with the field and radiation components. Therefore, Eq. (5) can be reformulated in terms of the temperature, using Eq. (4), yielding the following equation:

$$\dot{T} = \left(-HT + \frac{\Gamma_\phi \rho_\phi}{3s} \right) \left(\frac{dg_{\star s}(T)}{dT} \frac{T}{3g_{\star s}(T)} + 1 \right)^{-1}. \quad (7)$$

The above expression can be related to the energy density of radiation as $\rho_\gamma = \pi^2 g_\star(T) T^4/90$, with $g_\star(T)$ the degrees of freedom that contribute to the plasma energy density.

Approximated analytical solutions for Eqs. (5) and (6) can be straightforwardly obtained according to Ref. [43] as

$$\frac{\rho_\gamma(a)}{\rho_{\gamma,\text{ini}}} \simeq \left(\frac{a_{\text{ini}}}{a} \right)^4 + \frac{2}{8 - 3(\omega + 1)} \frac{\Gamma_\phi}{H_{\text{ini}}} \left(\frac{a_{\text{ini}}}{a} \right)^{\frac{3(\omega+1)}{2}}, \quad (8)$$

$$\frac{\rho_\phi(a)}{\rho_{\phi,\text{ini}}} \simeq \left(\frac{a_{\text{ini}}}{a} \right)^{3(\omega+1)} - \frac{2}{3(\omega + 1)} \frac{\Gamma_\phi}{H_{\text{ini}}} \left(\frac{a_{\text{ini}}}{a} \right)^{\frac{3(\omega+1)}{2}} \quad (9)$$

where the subscript ‘‘ini’’ refers to the energy density evaluated at the initial temperature $T_{\text{ini}} = m_\chi$. The above expressions are valid only when $\omega \neq -1$, as this value would indeterminate Eq. (9), and describe the behavior of both energy densities as a function of the scale factor. Notably, the evolution of ρ_ϕ is primarily governed by two terms: the first corresponds to the usual expression for the energy density of a barotropic fluid, while the second can be interpreted as a modification arising from its interaction with the radiation component. As the scale factor increases, the first term decreases more rapidly than the second, causing the fluid vanishes as the universe expands. It is important to mention that these expressions are approximate solutions and any occurrence of $\rho_\phi < 0$ is solely a result of the approximation. In the particular case where $\omega = -1$, the approximate analytical solution for ϕ takes the form:

$$\frac{\rho_\phi(a)}{\rho_{\phi,\text{ini}}} \simeq 1 + \frac{\Gamma_\phi}{H_{\text{ini}}} \ln \left(\frac{a_{\text{ini}}}{a} \right). \quad (10)$$

In this case, the energy density of the extra field does not decay but instead increases. This same behavior is observed for a phantom fluid, where $\omega < -1$, as can be seen from Eq. (9).

A notable aspect of incorporating the additional field ϕ is its potential influence on the inflation and reheating epochs, as explored in various studies [44, 46, 119–123]. In these works, it was proposed that the inflationary field could be represented by this field within the context of the NSC scenario, which roll down to its minimum to generate the reheat epoch. Conversely, several studies have examined scenarios where the additional field ϕ generates the reheating epoch without being associated with an inflationary field [26, 27, 33, 38]. However, it is crucial to emphasize that NSC scenarios must not alter the Big Bang Nucleosynthesis (BBN) epoch, given the highly accurate observations following this era, which are based

on the Λ CDM model [124–126]. Therefore, the new field must decay before the beginning of BBN, specifically at $T_{\text{end}} \gtrsim T_{\text{BBN}} \sim 4$ MeV. In the case of reheating, the same condition must be satisfied, meaning that T_{end} must be rename as T_{Rh} , which is the reheating temperature.

To estimate when a particle leaves the thermal bath, one must analyze whether its interactions are sufficiently efficient to keep it in equilibrium or if the universe’s expansion rate suppresses these interactions. Therefore, in the limit where $H = \Gamma_\phi$, the particle related to the ϕ -field will have completely decayed into SM plasma, being recovered the standard Λ CDM cosmology. This condition links the decay temperature with the decay rate through the relation

$$T_{\text{end}}^4 = \frac{90}{\pi^2 g_\star(T_{\text{end}})} M_p^2 \Gamma_\phi^2. \quad (11)$$

The addition of this new field introduces several key temperature parameters: T_{eq} , T_c , and T_{end} . T_{eq} represents the temperature at which the energy densities of ϕ and γ are equal, marking the transition point where ϕ begins to dominate over radiation. T_c denotes the temperature at which the decay of ϕ starts to significantly contribute to the entropy injection into ρ_γ . Finally, T_{end} is the temperature at which the field ϕ decays. Based on these definitions, we can identify four distinct regions: RI) $T_{\text{eq}} < T$, RII) $T_{\text{eq}} > T > T_c$, RIII) $T_c > T > T_{\text{end}}$, and RIV) $T < T_{\text{end}}$. Nevertheless, the last region is not of our interest, since it corresponds to the Λ CDM scenario, where ϕ has completely decayed. Consequently, the NSC scenario is characterized by the parameters $\kappa \equiv \rho_{\phi,\text{ini}}/\rho_{\gamma,\text{ini}}$, the temperature T_{end} , and the barotropic index ω . For illustration, Fig. 1 shows a NSC scenario with $\kappa = 10^{-2}$, $T_{\text{end}} = 7 \times 10^{-3}$ GeV, $m_\chi = 100$ GeV, and $\omega = 0$. For now on, the subscript ‘‘0’’ accounts for the current time.

Assuming constant degrees of freedom, the energy density of the field ϕ behaves as $\rho_\phi \propto a^{-3(\omega+1)}$. Otherwise, in regions I and II, where $T > T_c$, the temperature evolves as $T \propto a^{-1}$. Conversely, in region III, the temperature behaves as $T \propto a^{-3(\omega+1)/8}$. After the complete decay of ϕ , as it was shown in Eq. (9), the temperature takes the usual form $T \propto a^{-1}$, being recovered the Λ CDM cosmology. This behavior for the temperature is illustrated in Fig. 2 for a NSC scenario with $\kappa = 10^{-2}$, $T_{\text{end}} = 7 \times 10^{-3}$ GeV, $m_\chi = 100$ GeV, and $\omega = 0$. It is important to emphasize that the variations in temperature and radiation energy density are derived from the full numerical integration, which accounts for entropy and radiation degrees of freedom.

A. FIMPs in non-standard cosmologies

FIMPs are generated by a non-thermal production mechanism called Freeze-In. This DM genesis is based on the assumption that if the coupling of DM particles to the SM bath is small, meaning that their interactions with

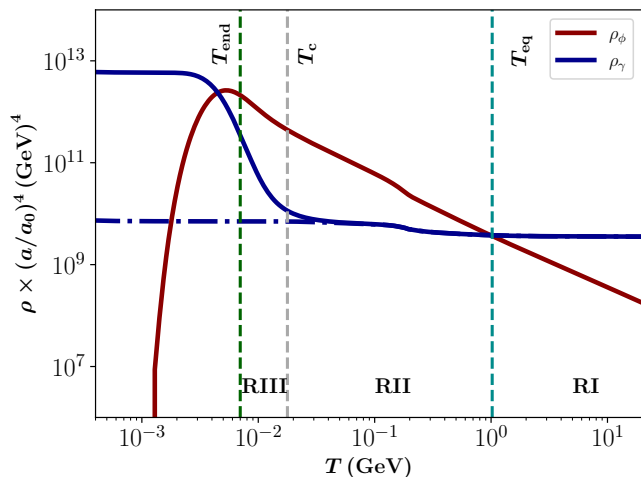


FIG. 1. Evolution of $\rho \times (a/a_0)^4$ as a function of the temperature T for $\kappa = 10^{-2}$, $T_{\text{end}} = 7 \times 10^{-3}$ GeV, $m_\chi = 100$ GeV, and $\omega = 0$. The solid lines correspond to the NSC scenario and the dashed-dotted line to the standard Λ CDM scenario, while the red line represents the new field ϕ and the blue lines the radiation component. The dashed lines correspond to the values of T_{eq} (cyan), T_c (grey), and T_{end} (green line).

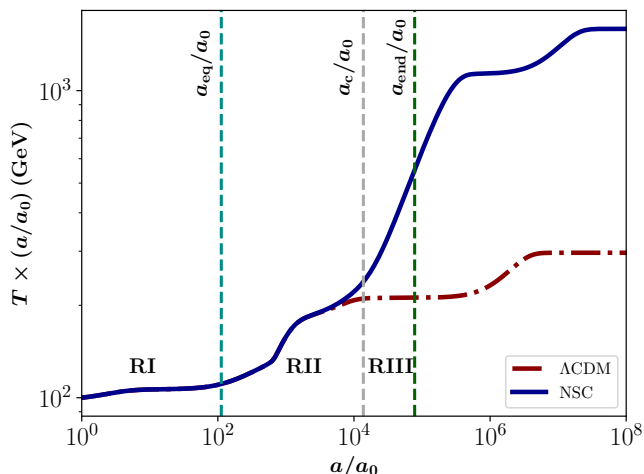


FIG. 2. Evolution of $T \times (a/a_0)$ as a function of a/a_0 for $\kappa = 10^{-2}$, $T_{\text{end}} = 7 \times 10^{-3}$ GeV, $m_\chi = 100$ GeV, and $\omega = 0$. The solid blue line represents the NSC scenario and the dashed-dotted red line the standard Λ CDM scenario. The dashed lines correspond to the values of T_{eq} (cyan), T_c (grey), and T_{end} (green line).

these particles are very feebly, then the DM particle never achieves the thermal equilibrium in the early universe with the bath particles. With the ongoing expansion of the universe, the production of FIMPs come to an end as their interaction rates become increasingly inefficient relative to the expansion rate of the universe, leading to the observed DM abundance. This means that these particles freeze their number, typically in $x \sim \mathcal{O}(1 \sim 5)$, where $x \equiv m_\chi/T$ is a dimensionless quantity.

These candidates can establish their abundance through two distinct mechanisms. The first one is UltraViolet (UV) freeze-in, and the second one is InfraRed (IR) freeze-in. In the UV freeze-in scenario, the process occurs when the mass of the mediator particle of the interaction with FIMPs exceeds the temperature of the thermal bath. This interaction involves higher-order, non-renormalizable operators, making it highly sensitive to the reheating temperature in the early universe. On the other hand, the IR freeze-in mechanism takes place at temperatures comparable to the mass of DM, through renormalizable operators.

To compute the DM relic density it is useful to define the Yield as $Y \equiv n_\chi/s$. An analytical solution to Eq. (3) for the IR freeze-in can be derived in the limit where $Y_{\text{eq}} \gg Y$, being obtained

$$Y \propto m_\chi \langle \sigma v \rangle, \quad (12)$$

solution that will be considered in our analysis since $\langle \sigma v \rangle$ is constant. It can be observed that larger values of the total thermal averaged annihilation cross-section increase the amount of DM, contrarily to the inversely proportional to $\langle \sigma v \rangle$ in the case of WIMP candidates.

In the case of the NSC, the decay of the new field, introduced at early times, generates an increment in the temperature of the universe and, consequently, in the entropy and radiation energy density. This change in the temperature can also be seen as a faster or slower expansion rate of the universe. The entropy injection can be parametrized by $D \equiv s(T_{\text{end}})/s(m_\chi) = (T_{\text{end}}/m_\chi)^3$, i.e., the entropy density before and after the decays of the new field ϕ . This left significant imprints in the DM production, considering that the Yield depends explicitly on the entropy density. Therefore, an increment in $s(T)$ will dilute the DM relic density. The latter means that DM parameters ($m_\chi, \langle \sigma v \rangle$) that overproduce the relic density in the Λ CDM model can, in the NSC scenario, reproduce the current DM relic density. The establishment of DM can occur in the four regions described in Section II:

- RI: In this region, the radiation component of the universe still dominates its expansion, i.e., $H \sim \sqrt{\rho_\gamma/3M_p^2} \propto T^2$ is almost the same as in the Λ CDM model. The condition $\kappa < 1$ ($\rho_{\gamma,\text{ini}} > \rho_{\phi,\text{ini}}$) is necessary for this region to exist. This behavior is illustrated in Fig. 3, for a NSC with $\kappa = 10^{-2}$, $T_{\text{end}} = 7 \times 10^{-3}$ GeV, $m_\chi = 100$ GeV, $\langle \sigma v \rangle = 5 \times 10^{-26}$ GeV $^{-2}$, and $\omega = 0$. It can be observed that the DM freezes its abundance before the decay of ϕ , and as the decays become significant, the DM relic density is diluted to reach its current value, allowing the parameters $(m_\chi, \langle \sigma v \rangle) = (100 \text{ GeV}, 5 \times 10^{-26} \text{ GeV}^{-2})$, which were previously ruled out in the Λ CDM scenario.
- RII: In this region, the expansion of the universe is dominated by the energy density of the field, i.e., $H \sim \sqrt{\rho_\phi/3M_p^2} \propto T^{3(\omega+1)/2}$. Fig. 4 shown the

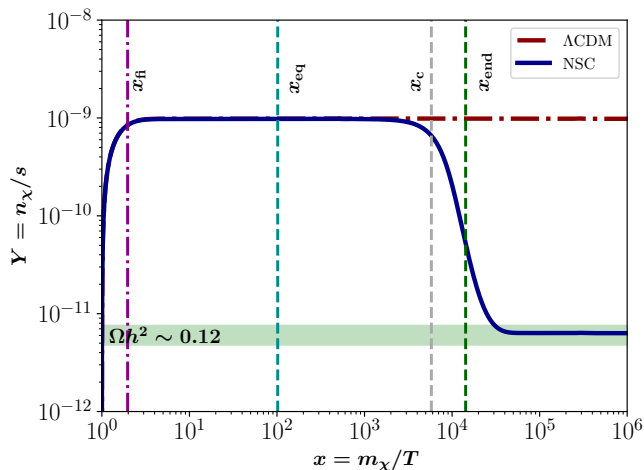


FIG. 3. Comparison in the yield production between the NSC (solid blue line) and the Λ CDM (dashed-dotted red line) scenarios for $\kappa = 10^{-2}$, $T_{\text{end}} = 7 \times 10^{-3}$ GeV, $m_\chi = 100$ GeV, $\langle\sigma v\rangle = 5 \times 10^{-26}$ GeV $^{-2}$, and $\omega = 0$. The dashed lines correspond to x_{eq} (cyan), x_c (grey), and x_{end} (green); while the dashed-dotted magenta line is the time when the DM candidate Freeze-In their number at x_{fi} . The green zone represents the current DM relic density according to Ref. [9], observing that the parameter space considered in this case gives us the right amount of DM in the NSC scenario.

evolution of the DM Yield for $\kappa = 1$, $T_{\text{end}} = 5 \times 10^{-2}$ GeV, $m_\chi = 100$ GeV, $\langle\sigma v\rangle = 10^{-24}$ GeV $^{-2}$, and $\omega = 0$. In this case, the freeze-in happens at different but closer times, and it can be seen that the DM Yield in the Λ CDM model is slightly higher than the NSC scenario. This is produced by the expansion rate of the universe different to $H \propto T^2$. Nevertheless, after the decay of ϕ , the entropy injection dilutes the DM relic density, bringing it to its current value.

- RIII: For this case, the universe expansion is still dominated by the ϕ field, but the decays begin to inject entropy to the SM bath. The expansion rate can be approximated as $H \sim \sqrt{\rho_\phi/3M_p^2} \propto T^4$, which means a decaying epoch. Fig. 5 shows the evolution of the DM Yield for $\kappa = 10^3$, $T_{\text{end}} = 2$ GeV, $m_\chi = 100$ GeV, $\langle\sigma v\rangle = 5 \times 10^{-22}$ GeV $^{-2}$, and $\omega = 0$. Once again, the particles freeze their abundance earlier in the NSC scenario compared to Λ CDM model, resulting in a lower DM yield. As the decay of ϕ becomes significant, the resulting entropy injection dilutes the DM relic density, bringing it to its present value.
- RIV: Finally, in this region the ϕ field has already fully decay and the Λ CDM model is recovered. This region is not of our interest.

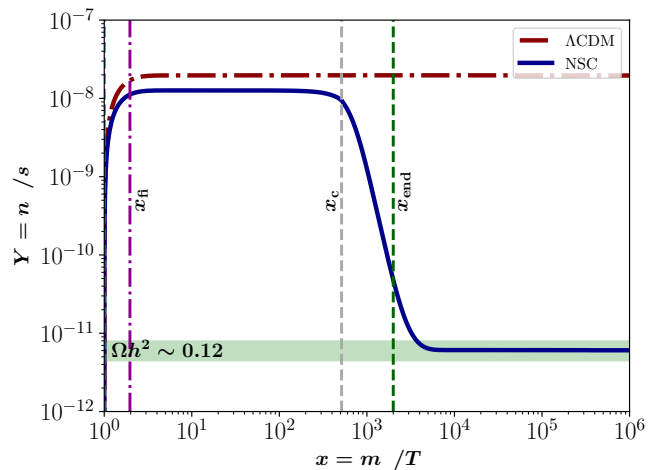


FIG. 4. Comparison in the yield production between the NSC (solid blue line) and the Λ CDM (dashed-dotted red line) scenarios for $\kappa = 1$, $T_{\text{end}} = 5 \times 10^{-2}$ GeV, $m_\chi = 100$ GeV, $\langle\sigma v\rangle = 10^{-24}$ GeV $^{-2}$, and $\omega = 0$. The dashed lines correspond to x_c (grey) and x_{end} (green), while the dashed-dotted magenta line is the time when the DM candidate Freeze-In their number at x_{fi} . The green zone represents the current DM relic density according to Ref. [9], observing that the parameter space considered in this case gives us the right amount of DM in the NSC scenario.

III. BULK VISCOUS NON-STANDARD COSMOLOGIES

Bulk viscous NSCs were studied for the first time in Ref. [118]. However, to ensure the self-consistency of our study, we will revisit this former work.

The equations that rule the universe evolution are obtained through the Einstein's equations

$$R_{\mu\nu} - \frac{1}{2}Rg_{\mu\nu} + \Lambda g_{\mu\nu} = \frac{1}{M_p^2}T_{\mu\nu}, \quad (13)$$

where $R_{\mu\nu}$ is the Ricci tensor, R the Ricci scalar, $g_{\mu\nu}$ is the metric tensor of the four-dimensional spacetime, $T_{\mu\nu}$ is the total energy-momentum tensor, and Λ the cosmological constant. In the NSC scenario, analogous to the classical description of the universe, the total energy budget is characterized by a perfect fluid, whose corresponding energy-momentum tensor can be expressed as follows:

$$T_{\mu\nu} = p_t g_{\mu\nu} + (\rho_t + p_t) u_\mu u_\nu, \quad (14)$$

where u_μ correspond to the four-velocity of the fluid element. Hence, for the spatially flat Friedmann-Lemaitre-Robertson-Walker (FLRW) metric, given by

$$dl^2 = -dt^2 + a^2(t) (dr^2 + r^2 d\vartheta^2 + r^2 \sin^2(\vartheta) d\varphi^2), \quad (15)$$

we obtain the Friedmann Eq. (1) and the acceleration equation

$$2\dot{H} + 3H^2 = -p_t. \quad (16)$$

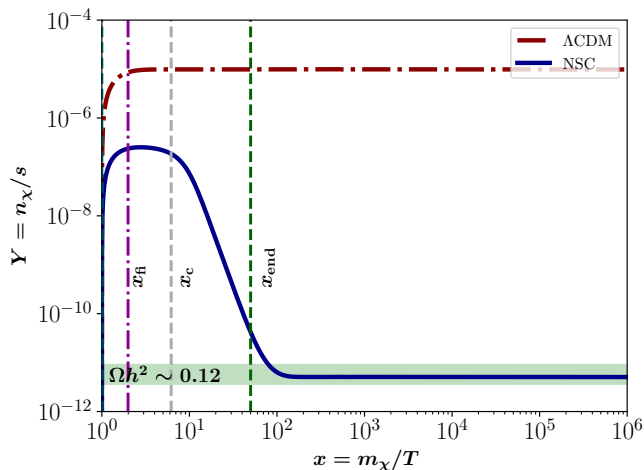


FIG. 5. Comparison in the yield production between the NSC (solid blue line) and the Λ CDM (dashed-dotted red line) scenarios for $\kappa = 10^3$, $T_{\text{end}} = 2$ GeV, $m_\chi = 100$ GeV, $\langle\sigma v\rangle = 5 \times 10^{-22}$ GeV $^{-2}$, and $\omega = 0$. The dashed lines correspond to x_c (grey) and x_{end} (green), while the dashed-dotted magenta line is the time when the DM candidate Freeze-In their number at x_{fi} . The green zone represents the current DM relic density according to Ref. [9], observing that the parameter space considered in this case gives us the right amount of DM in the NSC scenario.

In the above expression, we have disregarded the cosmological constant, as it is negligible compared to the other fluids during the epoch of interest. In this procedure, the continuity equation (2) is derived from the expression $\nabla^\nu T_{\mu\nu} = 0$.

To incorporate non-perfect fluids into the model, we specifically use the relativistic thermodynamic framework out of equilibrium of Eckart. This theory introduces a small correction $\Delta T_{\mu\nu}$ to Eq. (14), expressed as $\Delta T_{\mu\nu} = -3H\xi(g_{\mu\nu} + u_\mu u_\nu)$ [56], where ξ is the bulk viscosity. In particular, we assume that the dissipative fluid does not experience heat flow or shear viscosity. Hence, the energy-momentum tensor can be written as

$$T_{\mu\nu} = P_{\text{eff}} g_{\mu\nu} + (\rho + P_{\text{eff}}) u_\mu u_\nu, \quad (17)$$

where $P_{\text{eff}} = p_t + \Pi$, with $\Pi = -3H\xi$ the bulk viscous pressure. Then, Eqs. (2) and (16), take the form

$$2\dot{H} + 3H^2 = -p_t - \Pi, \quad (18)$$

$$\dot{\rho}_t + 3H(\rho_t + p_t + \Pi) = 0, \quad (19)$$

while Eq. (1) remains unchanged. It is important to note that bulk viscosity influences the evolution of the universe through the bulk viscous pressure. In particular, for an expanding universe, the expression $\Pi = -3H\xi$ is always negative ($\xi > 0$ to maintain consistency with the second law of thermodynamics [127]). Consequently, this viscosity leads to an acceleration in the expansion of the universe, as can be seen from Eq. (18). In agreement with this, an interesting case is presented in Ref. [128],

where the interaction term of the classical NSC scenario can be effectively interpreted as a time-dependent dissipation.

Taking into account that the division of the total energy budget of the universe into distinct components is purely conventional, as the energy-momentum tensor describes all fluid components as a whole, then we can express the effective pressure for this NSC as $P_{\text{eff}} = p_\gamma + p_\phi + p_\chi + \Pi$, where we can identify $P_{\text{eff},\phi} = p_\phi + \Pi$. In other words, the field ϕ represents the fluid that undergoes dissipative processes during its cosmic evolution, and Eq. (6) becomes

$$\dot{\rho}_\phi + 3(\omega + 1)H\rho_\phi = -\Gamma_\phi\rho_\phi - 3H\Pi, \quad (20)$$

as the other equations relevant to the NSC scenario remain unchanged. In this context, bulk viscosity can depend on the temperature and pressure of the dissipative fluid [127]. Hence, a natural and most extensively studied expression for the bulk viscosity is to assume a proportional dependence to the power of its energy density, $\xi = \xi_0\rho_\phi^{1/2}$, where $\xi_0 = \hat{\xi}_0 M_p$, allowing $\hat{\xi}_0$ to be a dimensionless parameter. With this consideration, Eq. (20) takes the form

$$\dot{\rho}_\phi + 3(\omega + 1)H\rho_\phi = -\Gamma_\phi\rho_\phi + 9M_p\hat{\xi}_0 H^2\rho_\phi^{1/2}. \quad (21)$$

It is important to highlight that the chosen parameterization for the bulk viscosity has the advantage that, once the field ϕ fully decays into SM plasma, the dissipation becomes negligible and we recover the standard Λ CDM scenario without viscosity. Therefore, to compare the classical NSC scenario with its bulk viscous counterpart, we numerically integrate Eqs. (1), (3), (6), (7), and (21). The results of this analysis are presented in the following subsection.

A. Comparison between scenarios

In this section, we will compare all the features discussed in Sections II and III, between the NSC and the bulk viscous NSC scenarios.

In Fig. 6, we depict the evolution of $\rho \times (a/a_0)^4$ as a function of the temperature T for $\kappa = 10^{-3}$, $T_{\text{end}} = 7 \times 10^{-3}$ GeV, $\hat{\xi}_0 = 10^{-2}$, $m_\chi = 100$ GeV, and $\omega = 0$. The solid and dashed-dotted lines correspond to the NSC with and without bulk viscosity, respectively; while the red lines represent the new field ϕ and the blue lines the radiation component. We also depict the values of T_{eq} (cyan), T_c (grey), and T_{end} (green) for the NSC with bulk viscosity (dashed lines) and the classical NSC (dotted lines). From the figure, it can be observed that the bulk viscous NSC leads to an enhanced production of the field ϕ compared to the classical NSC scenario, resulting in a greater increase in the radiation energy density due to the decay of the field, and consequently, a higher entropy injection into the SM bath. An interesting feature is that the overall temperature-dependent behavior

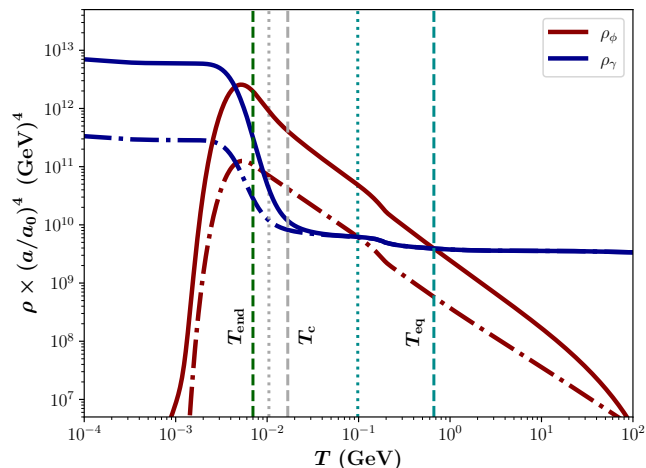


FIG. 6. Evolution of $\rho \times (a/a_0)^4$ as a function of the temperature T for $\kappa = 10^{-3}$, $T_{\text{end}} = 7 \times 10^{-3}$ GeV, $\hat{\xi}_0 = 10^{-2}$, $m_\chi = 100$ GeV, and $\omega = 0$. The solid and dashed-dotted lines correspond to the NSC with and without bulk viscosity, respectively; while the red lines represent the new field ϕ and the blue lines the radiation component. We also depict the values of T_{eq} (cyan), T_c (grey), and T_{end} (green) for the NSC with bulk viscosity (dashed lines) and the classical NSC (dotted lines).

of the fluids remains largely unchanged between the two scenarios, allowing us to conclude that the field ϕ becomes negligible in the bulk viscous NSC scenario as in the classical NSC according to Eq. (9). Nevertheless, this conclusion is only valid for bulk viscous NSC models with $\omega > -1$, since viscosity can lead to obtaining an effective barotropic index where $\omega_{\text{eff}} \leq -1$ for an $\omega > -1$ but close to -1 , i.e., we can obtain a behavior where the field ϕ never decays. Meanwhile, Figure 7 shows the comparison in the yield production between the classical NSC (solid red line) and the NSC with bulk viscosity (solid blue line) for the same values of κ , T_{end} , $\hat{\xi}_0$, m_χ , and ω as in Figure 6, considering $\langle \sigma v \rangle = 5 \times 10^{-26}$ GeV $^{-2}$. The dashed and dotted lines correspond to x_{eq} (cyan), x_c (grey), and x_{end} (green) for the NSC with and without bulk viscosity, respectively; while the dashed-dotted magenta line is the time when the DM candidate Freeze-In their number at x_{fi} . The green zone represents the current DM relic density according to Ref. [9]. Firstly, note that the lines for x_{end} and x_{fi} are the same for both models. Secondly, note that the behavior of the Yield production is the same in both models until the decay of ϕ . After that, it is observed that the higher entropy injection generated by the viscous term leads to lower values of the DM Yield. This means that the DM relic density agrees with the current observation for a NSC with bulk viscosity in contrast with the standard NSC case which overproduces the DM relic density.

The comparison in the parameter space of the NSC models, namely κ and T_{end} , with a fixed ω , is depicted in Figures 8, 9, and 10. The figures were obtained for

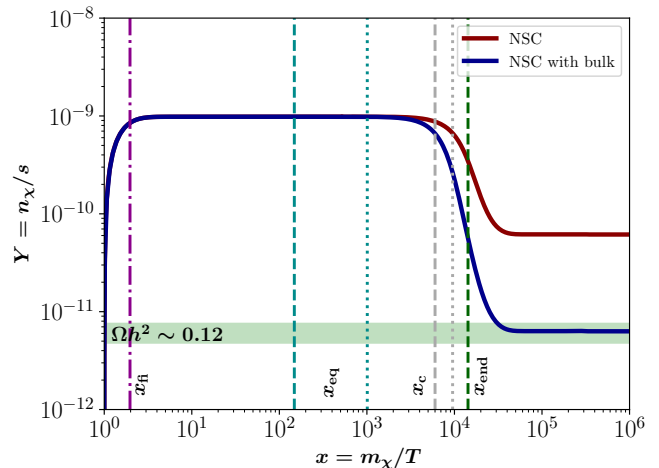


FIG. 7. Comparison in the yield production between the classical NSC (solid red line) and the NSC with bulk viscosity (solid blue line) for $\kappa = 10^{-3}$, $T_{\text{end}} = 7 \times 10^{-3}$ GeV, $\hat{\xi}_0 = 10^{-2}$, $m_\chi = 100$ GeV, $\langle \sigma v \rangle = 5 \times 10^{-26}$ GeV $^{-2}$, and $\omega = 0$. The dashed and dotted lines correspond to x_{eq} (cyan), x_c (grey), and x_{end} (green) for the NSC with and without bulk viscosity, respectively; while the dashed-dotted magenta line is the time when the DM candidate Freeze-In their number at x_{fi} . The green zone represents the current DM relic density according to Ref. [9], observing that the parameter space considered in this case gives us the right amount of DM in the bulk viscous NSC scenario.

the values $\hat{\xi}_0 = 10^{-2}$, $m_\chi = 100$ GeV, and $\langle \sigma v \rangle = 10^{-26}$ GeV $^{-2}$. The solid red and blue lines correspond to the parameter space that reproduces the current DM relic density for the classical NSC and the NSC with bulk viscosity, respectively. We also delimit the three regions of interest (see Section II A) through the equalities $T_{\text{eq}} = T_{\text{fi}}$ (cyan), $T_c = T_{\text{fi}}$ (grey), and $T_{\text{end}} = T_{\text{fi}}$ (green) for the NSC with bulk viscosity (dashed lines) and the classical NSC (dashed-dotted lines). The red and blue zones represent their respective parameter space in which $\rho_\phi < \rho_\gamma$, $\forall t$, i.e., the regions in which the Hubble parameter is always approximately similar to the Λ CDM model ($H \sim T^2$). The grey zone corresponds to the forbidden BBN epoch that starts at $T_{\text{BBN}} \sim 4 \times 10^{-3}$ GeV. In Figure 8, obtained for $\omega = 0$, it can be seen that for higher values of κ and T_{end} (RIII), the parameter space is slightly the same, meanwhile in RII the curves separate from each other. However, the greatest differences between the NSC with and without bulk viscosity cases are presented in RI, exhibiting an approximate independent behavior of the κ parameter, which can be explained by the dominance of the viscous term over the decaying term. On the other hand, Figure 9, obtained for $\omega = -2/5$, exhibits a similar behavior to the $\omega = 0$ case, with the difference that the approximate independent κ values in RI are reached to higher temperatures and, therefore, there is a smaller window of T_{end} to reproduce the current DM relic density. Finally, in Figure

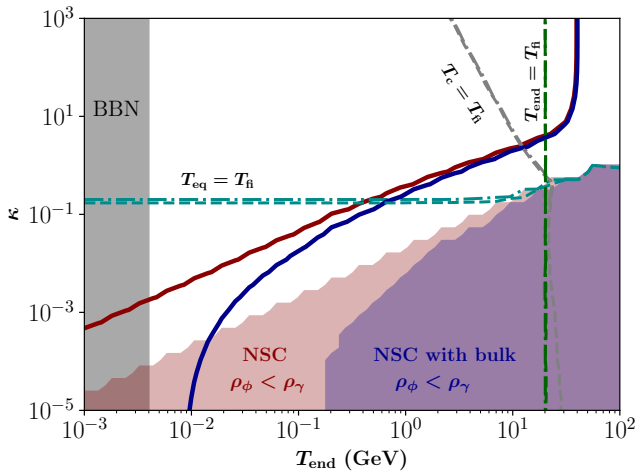


FIG. 8. Parameter space (T_{end}, κ) for the NSC models with $\hat{\xi}_0 = 10^{-2}$, $m_\chi = 100$ GeV, $\langle\sigma v\rangle = 10^{-26}$ GeV $^{-2}$, and $\omega = 0$. The solid red and blue lines correspond to the parameter space that reproduces the current DM relic density for the classical NSC and the NSC with bulk viscosity, respectively. We also delimit the three regions of interest through the equalities $T_{\text{eq}} = T_{\text{fi}}$ (cyan), $T_c = T_{\text{fi}}$ (grey), and $T_{\text{end}} = T_{\text{fi}}$ (green) for the NSC with bulk viscosity (dashed lines) and the classical NSC (dashed-dotted lines). The red and blue zones represent their respective parameter space in which $\rho_\phi < \rho_\gamma$, $\forall t$. The grey zone corresponds to the forbidden BBN epoch that starts at $T_{\text{BBN}} \sim 4 \times 10^{-3}$ GeV. Note that the bulk viscous NSC scenario allows the model to take lower values of κ .

10, obtained for $\omega = 2/5$, there is no existence of RI since the values of κ are greater than 1. In other words, $\rho_{\phi,\text{ini}}$ is always greater than $\rho_{\gamma,\text{ini}}$. The parameters for NSC with and without bulk viscosity are very close (less than one order of magnitude) and, therefore, the FIMP DM candidates are not so sensitive to the inclusion of the bulk viscosity when the value of ω is higher compared these two cosmological scenarios. This also explains the absence of the red and blue zones, and the lines for T_{eq} , T_c , and T_{end} .

Last but not least, Figure 11 shows the FIMP DM candidate parameter space, namely m_χ and $\langle\sigma v\rangle$, for $\kappa = 10^{-3}$, $T_{\text{end}} = 7 \times 10^{-3}$ GeV, $\hat{\xi}_0 = 10^{-2}$, and $\omega = 0$. The solid red and blue lines correspond to the parameter space that reproduces the current DM relic density for the classical NSC and the NSC with bulk viscosity, respectively. The red and blue zones represent their respective parameter space in which $\rho_\phi < \rho_\gamma$, $\forall t$. From the figure, a similar behavior can be observed between the two scenarios for small values of FIMP DM candidate mass and high values of the thermal average annihilation cross-section (and vice-versa). Also, there is a gap between the curves, shifting the case with bulk viscosity upward with respect to the standard NSC scenario, reaching larger values of $\langle\sigma v\rangle$ (approximately two orders of magnitude) in the same range of m_χ .

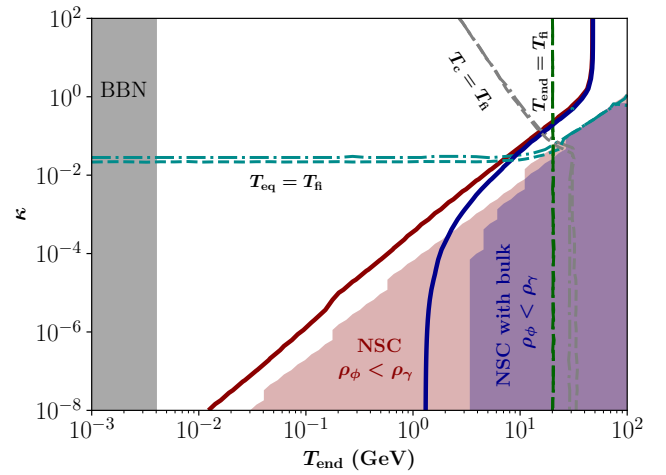


FIG. 9. Parameter space (T_{end}, κ) for the NSC models with $\hat{\xi}_0 = 10^{-2}$, $m_\chi = 100$ GeV, $\langle\sigma v\rangle = 10^{-26}$ GeV $^{-2}$, and $\omega = -2/5$. The solid red and blue lines correspond to the parameter space that reproduces the current DM relic density for the classical NSC and the NSC with bulk viscosity, respectively. We also delimit the three regions of interest through the equalities $T_{\text{eq}} = T_{\text{fi}}$ (cyan), $T_c = T_{\text{fi}}$ (grey), and $T_{\text{end}} = T_{\text{fi}}$ (green) for the NSC with bulk viscosity (dashed lines) and the classical NSC (dashed-dotted lines). The red and blue zones represent their respective parameter space in which $\rho_\phi < \rho_\gamma$, $\forall t$. The grey zone corresponds to the forbidden BBN epoch that starts at $T_{\text{BBN}} \sim 4 \times 10^{-3}$ GeV.

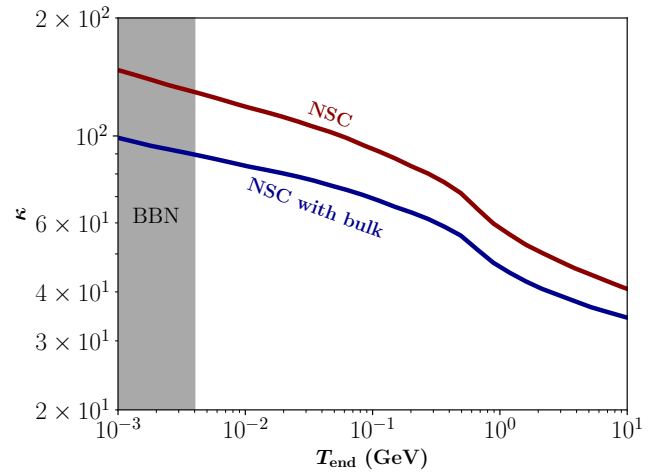


FIG. 10. Parameter space (T_{end}, κ) for the NSC models with $\hat{\xi}_0 = 10^{-2}$, $m_\chi = 100$ GeV, $\langle\sigma v\rangle = 10^{-26}$ GeV $^{-2}$, and $\omega = 2/5$. The solid red and blue lines correspond to the parameter space that reproduces the current DM relic density for the classical NSC and the NSC with bulk viscosity, respectively. The grey zone represents the forbidden BBN epoch that starts at $T_{\text{BBN}} \sim 4 \times 10^{-3}$ GeV. Note that the bulk viscous NSC scenario allows the model to take lower values of κ .

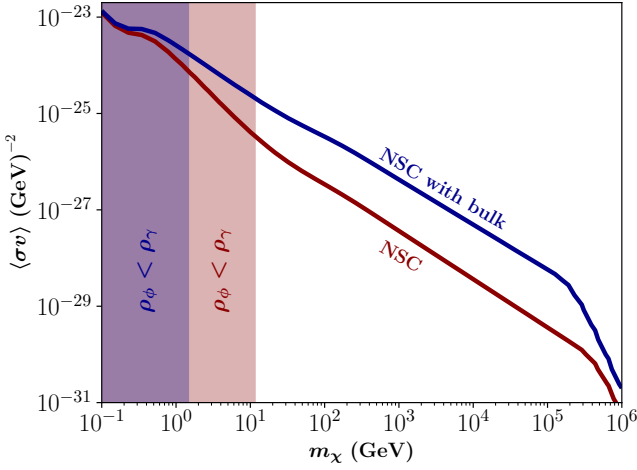


FIG. 11. Parameter space $(m_\chi, \langle\sigma v\rangle)$ for the FIMP DM candidate with $\kappa = 10^{-3}$, $T_{\text{end}} = 7 \times 10^{-3}$ GeV, $\hat{\xi}_0 = 10^{-2}$, and $\omega = 0$. The solid red and blue lines correspond to the parameter space that reproduces the current DM relic density for the classical NSC and the NSC with bulk viscosity, respectively. The red and blue zones represent their respective parameter space in which $\rho_\phi < \rho_\gamma, \forall t$. Note that the bulk viscous NSC scenario allows to achieve larger values of $\langle\sigma v\rangle$.

B. Parameter spaces in the bulk viscous non-standard cosmologies

From now on, we focus the analysis on the study of the parameter spaces (T_{end}, κ) of the model and $(m_\chi, \langle\sigma v\rangle)$ of the FIMP DM candidate for the bulk viscous NSC scenario alone.

In Figure 12, we depict the parameter space (T_{end}, κ) for $\hat{\xi}_0 = 10^{-2}$, $\langle\sigma v\rangle = 10^{-22}$ GeV $^{-2}$, and $\omega = 0$. The solid blue, red, and green lines correspond to the parameter space that reproduces the current DM relic density for $m_\chi = 10^4$, 10^2 , and 1 GeV, respectively. The green and red zones represent the parameter space in which $\rho_\phi < \rho_\gamma, \forall t$, for $m_\chi = 1$ and 10^2 GeV, respectively. The grey zone corresponds to the forbidden BBN epoch that starts at $T_{\text{BBN}} \sim 4 \times 10^{-3}$ GeV. From the figure, it can be observed that lower values of m_χ shift the curves downward to the left, while the regions in which $\rho_\phi < \rho_\gamma$ are shifted upward to the left. Hence, the blue zone is achieved at higher values of T_{end} and lower values of κ . Interestingly, for $m_\chi = 10^4$ GeV, exists a region in which the curve that reproduces the current DM relic density goes to higher values of κ . While this behavior occurs in the forbidden BBN zone, this parameter space may be accessible for higher values of the DM mass. Otherwise, Figure 13 shows the same parameter space as Figure 12 for $\hat{\xi}_0 = 10^{-2}$, $m_\chi = 100$ GeV, and $\omega = 0$. The solid blue, red, and green lines correspond to the parameter space that reproduces the current DM relic density for $\langle\sigma v\rangle = 10^{-22}$, 10^{-24} , and 10^{-26} GeV $^{-2}$, respectively. The grey zones represent the parameter space in which $\rho_\phi < \rho_\gamma, \forall t$ (for the three cases), and the forbidden BBN

epoch. As it can be noted, a decrease in the values for the thermal average annihilation cross-section shifts the parameters that reproduce the current DM relic density downward to the right, allowing access to the “approximated independent κ -zone” described in Section III A. Also, it is interesting to analyze the behavior of varying the DM mass (Figure 12) and its interactions (Figure 13). For instance, for higher values of m_χ appear a zone allowed to reproduce the current DM relic density in which the values of κ increase when T_{end} is decreasing. On the other hand, smaller values of $\langle\sigma v\rangle$ allow lower values of κ when T_{end} is diminishing up to the independent zone mentioned above. Finally, Figure 14 shows the parameter space mentioned before for $m_\chi = 100$ GeV, $\langle\sigma v\rangle = 10^{-22}$ GeV $^{-2}$, and $\omega = 0$. The solid green, red, blue and magenta lines correspond to the parameter space that reproduces the current DM relic density for $\hat{\xi}_0 = 10^{-3}$, 2.5×10^{-2} , 5×10^{-2} and 10^{-1} , respectively. The green, red, and blue zones represent their respective parameter space in which $\rho_\phi < \rho_\gamma, \forall t$. As before, the grey zone corresponds to the forbidden BBN epoch. As it is possible to see, higher values of $\hat{\xi}_0$ shift the curves and the regions, in which $\rho_\phi < \rho_\gamma$, downward to the right. Hence, the magenta zone is achieved at higher values of T_{end} and lower values of κ . Also, this increment in the $\hat{\xi}_0$ -values generates more prominent curvatures in the “approximately independent κ -zone”, reducing the T_{end} parameter space that could reproduce the current DM relic density.

The above discussion shows how certain values of m_χ and $\langle\sigma v\rangle$ open the possibility to new combinations of (T_{end}, κ) parameters to reproduce the current DM relic density and how combining different DM parameters could reach higher or lower values in the model parameters. For instance, for higher values of $\hat{\xi}_0$ and small values of $\langle\sigma v\rangle$ it is possible to access small values for κ and shorter range for T_{end} . Meanwhile, a large range of T_{end} and lower values of κ could be reached for small values of $(m_\chi, \langle\sigma v\rangle)$ and higher values of $\hat{\xi}_0$.

On the other hand, in Figure 15, we depict the parameter space $(m_\chi, \langle\sigma v\rangle)$ for $T_{\text{end}} = 7 \times 10^{-3}$ GeV, $\hat{\xi}_0 = 10^{-2}$, and $\omega = 0$. The solid green, red, and blue lines correspond to the parameter space that reproduces the current DM relic density for $\kappa = 1$, 10^{-1} , and 10^{-3} , respectively. The blue zone represents the parameter space in which $\rho_\phi < \rho_\gamma, \forall t$, for $\kappa = 10^{-3}$. From the figure, it can be observed that higher values of κ shift the curves upward, reaching larger values of $\langle\sigma v\rangle$ in the same DM mass range. Otherwise, Figure 16 shows the same parameter space as Figure 15 for $\kappa = 10^{-3}$, $\hat{\xi}_0 = 10^{-2}$, and $\omega = 0$. The solid green, red, and blue lines correspond to the parameter space that reproduces the current DM relic density for $T_{\text{end}} = 7 \times 10^{-3}$, 10^{-1} , and 1 GeV, respectively. The blue and red zones represent the parameter space in which $\rho_\phi < \rho_\gamma, \forall t$, for $T_{\text{end}} = 1$ and 10^{-1} GeV, respectively. As it can be noted, an increment in the T_{end} -values shifts downward to the right of the parameter space that reproduces the DM relic density, reaching smaller values of $\langle\sigma v\rangle$ in the same m_χ range. Note that the regions in

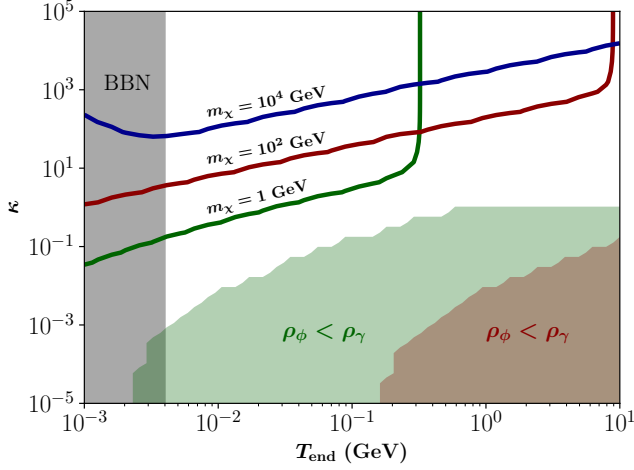


FIG. 12. Parameter space (T_{end}, κ) for the bulk viscous NSC with $\hat{\xi}_0 = 10^{-2}$, $\langle\sigma v\rangle = 10^{-22}$ GeV $^{-2}$, and $\omega = 0$. The solid blue, red, and green lines correspond to the parameter space that reproduces the current DM relic density for $m_\chi = 10^4$, 10^2 , and 1 GeV, respectively. The green and red zones represent the parameter space in which $\rho_\phi < \rho_\gamma, \forall t$, for $m_\chi = 1$ and 10^2 GeV, respectively. The grey zone corresponds to the forbidden BBN epoch that starts at $T_{\text{BBN}} \sim 4 \times 10^{-3}$ GeV. Note that lower values of m_χ allow the model to take lower values of κ .

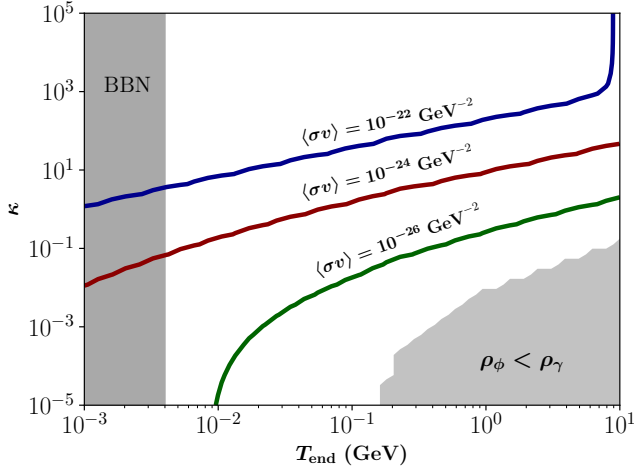


FIG. 13. Parameter space (T_{end}, κ) for the bulk viscous NSC with $\hat{\xi}_0 = 10^{-2}$, $m_\chi = 100$ GeV, and $\omega = 0$. The solid blue, red, and green lines correspond to the parameter space that reproduces the current DM relic density for $\langle\sigma v\rangle = 10^{-22}$, 10^{-24} , and 10^{-26} GeV $^{-2}$, respectively. The grey zones represent the parameter space in which $\rho_\phi < \rho_\gamma, \forall t$ (for the three cases), and the forbidden BBN epoch that starts at $T_{\text{BBN}} \sim 4 \times 10^{-3}$ GeV. Note that a decrease in the total thermal averaged annihilation cross-section allows the model to take lower values of κ .

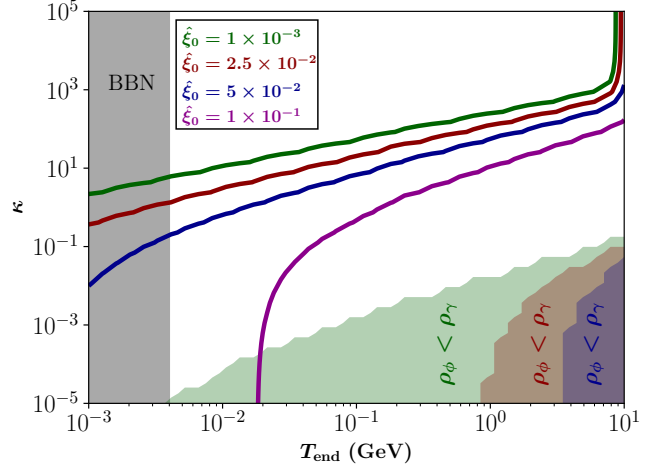


FIG. 14. Parameter space (T_{end}, κ) for the bulk viscous NSC with $m_\chi = 100$ GeV, $\langle\sigma v\rangle = 10^{-22}$ GeV $^{-2}$, and $\omega = 0$. The solid green, red, blue and magenta lines correspond to the parameter space that reproduces the current DM relic density for $\hat{\xi}_0 = 10^{-3}$, 2.5×10^{-2} , 5×10^{-2} and 10^{-1} , respectively. The green, red, and blue zones represent their respective parameter space in which $\rho_\phi < \rho_\gamma, \forall t$. The grey zone corresponds to the forbidden BBN epoch that starts at $T_{\text{BBN}} \sim 4 \times 10^{-3}$ GeV. Note that higher values of $\hat{\xi}_0$ allow the model to take lower values of κ .

which $\rho_\phi < \rho_\gamma$ are shifted to the right and, therefore, the green zone is achieved at lower values of m_χ . Finally, Figure 17 shows the parameter space mentioned before for $\kappa = 10^{-3}$, $T_{\text{end}} = 7 \times 10^{-3}$ GeV, and $\omega = 0$. The solid magenta, blue, red, and green lines correspond to the parameter space that reproduces the current DM relic density for $\hat{\xi}_0 = 10^{-1}$, 5×10^{-2} , 2.5×10^{-2} , and 10^{-3} , respectively. The blue, red, and green zones represent the parameter space in which $\rho_\phi < \rho_\gamma, \forall t$, for $\hat{\xi}_0 = 5 \times 10^{-2}$, 2.5×10^{-2} , and 10^{-3} , respectively. As it is possible to see, higher values of $\hat{\xi}_0$ shift the curves upward, reaching larger values of $\langle\sigma v\rangle$. Also, this increment generates a more prominent slope due to the bulk viscosity term. In this case, the regions in which $\rho_\phi < \rho_\gamma$ are shifted to the left and, therefore, the magenta zone is achieved at lower values of m_χ .

The aforementioned shows how certain parameters of the bulk viscosity NSC vary the FIMP DM candidates parameters to reproduce the current DM relic density. For instance, a combination of small values for $\hat{\xi}_0$, κ , and T_{end} could reach smaller values for $\langle\sigma v\rangle$ and a shorter range for m_χ . On the other hand, for stronger DM interaction, it is useful to increase the value of the quantities $\hat{\xi}_0$, κ , and T_{end} , which also expands the DM mass range. Notice that the bulk viscous term dominates in these shifts for the DM parameter space.

Last but not least, we present in Figure 18 the parameter space $(m_\chi, \langle\sigma v\rangle)$ for the FIMP DM candidate with $T_{\text{end}} = 7 \times 10^{-3}$ GeV and $\hat{\xi}_0 = 10^{-2}$. The solid red, blue, green, and magenta lines correspond to the parameter

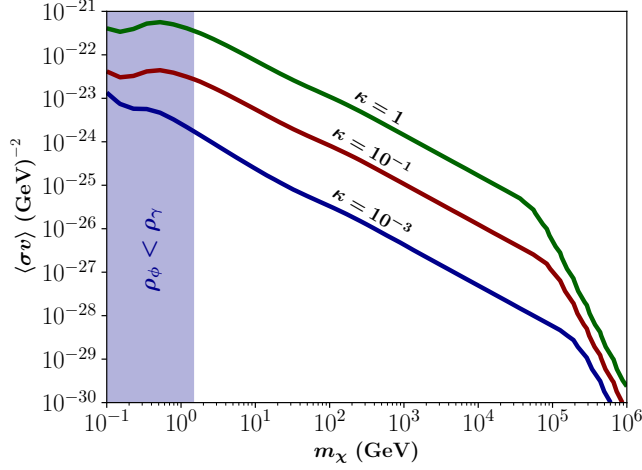


FIG. 15. Parameter space $(m_\chi, \langle\sigma v\rangle)$ for the FIMP DM candidate with $T_{\text{end}} = 7 \times 10^{-3}$ GeV, $\hat{\xi}_0 = 10^{-2}$, and $\omega = 0$. The solid green, red, and blue lines correspond to the parameter space that reproduces the current DM relic density for $\kappa = 1$, 10^{-1} , and 10^{-3} , respectively. The blue zone represents the parameter space in which $\rho_\phi < \rho_\gamma$, $\forall t$, for $\kappa = 10^{-3}$. Note that a decrease in the κ -values allow to achieve smaller values of $\langle\sigma v\rangle$.

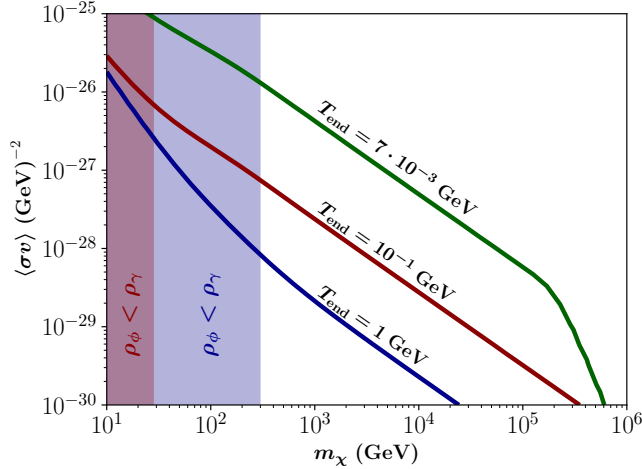


FIG. 16. Parameter space $(m_\chi, \langle\sigma v\rangle)$ for the FIMP DM candidate with $\kappa = 10^{-3}$, $\hat{\xi}_0 = 10^{-2}$, and $\omega = 0$. The solid green, red, and blue lines correspond to the parameter space that reproduces the current DM relic density for $T_{\text{end}} = 7 \times 10^{-3}$, 10^{-1} , and 1 GeV, respectively. The blue and red zones represent the parameter space in which $\rho_\phi < \rho_\gamma$, $\forall t$, for $T_{\text{end}} = 1$ and 10^{-1} GeV, respectively. Note that higher values of T_{end} allow to achieve smaller values of $\langle\sigma v\rangle$.

space that reproduces the current DM relic density for $\omega = -1/5$, 0, 1, and $1/3$, respectively. The blue and red zones represent the parameter space in which $\rho_\phi < \rho_\gamma$, $\forall t$, for $\omega = 0$ and $-1/5$, respectively. For illustrative purposes, the curves corresponding to $\omega = -1/5$ and $\omega = 0$ were obtained with $\kappa = 10^{-3}$, while the curve for $\omega = 1/3$

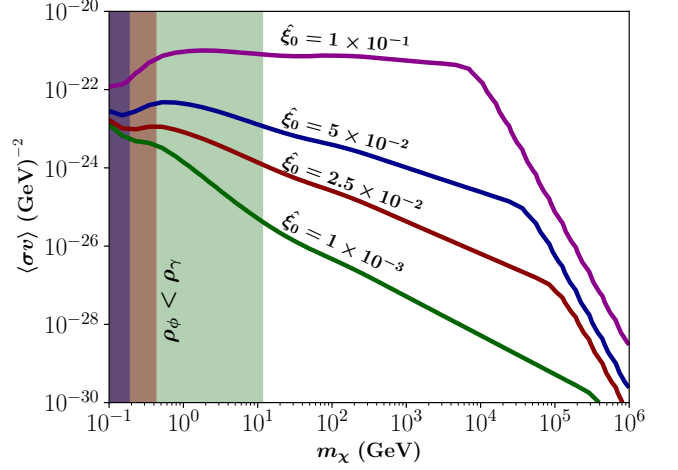


FIG. 17. Parameter space $(m_\chi, \langle\sigma v\rangle)$ for the FIMP DM candidate with $\kappa = 10^{-3}$, $T_{\text{end}} = 7 \times 10^{-3}$ GeV, and $\omega = 0$. The solid magenta, blue, red, and green lines correspond to the parameter space that reproduces the current DM relic density for $\hat{\xi}_0 = 10^{-1}$, 5×10^{-2} , 2.5×10^{-2} , and 10^{-3} , respectively. The blue, red, and green zones represent the parameter space in which $\rho_\phi < \rho_\gamma$, $\forall t$, for $\hat{\xi}_0 = 5 \times 10^{-2}$, 2.5×10^{-2} , and 10^{-3} , respectively. Note that higher values of $\hat{\xi}_0$ allow to achieve larger values of $\langle\sigma v\rangle$.

was obtained using $\kappa = 1$, and the curve for $\omega = 1$ with $\kappa = 10^3$. Notice that small values of ω can be interpreted as a counterclockwise rotation (and vice versa), leading to a maximum $\langle\sigma v\rangle$ in the cases with small values of ω . On the other hand, the larger range for m_χ is reaching for the case $\omega = 0$ (CDM or dust case). Also, it was shown that larger values in κ shift the curves upward. This last possibly explains why the parameters that reproduce the current DM relic density for $\omega = 1/3$ (radiation) are below $\omega = 1$ (kination or stiff matter). It is important to mention that this analysis must be taken carefully because some curves were obtained using different values of κ .

IV. CONCLUSIONS

In this paper, we revisit the bulk viscous NSC scenario studied in [118] in which the early universe is dominated by two interacting fluids, namely the new field ϕ and radiation, by considering that ϕ experiences dissipative processes during their cosmic evolution in the form of bulk viscosity. Working in the framework of Eckart's theory for non-perfect fluids, we consider an interaction term of the form $\Gamma_\phi \rho_\phi$ and a bulk viscosity described by the expression $\xi = \xi_0 \rho_\phi^{1/2}$. The latter has the advantage that when the field fully decays due to the interaction, the dissipation is negligible, and the standard Λ CDM cosmology is fully recovered. Also, when $\xi_0 \rightarrow 0$, we recover the classical NSC scenario. Following the same scheme as in [118], we investigate the parameter space that can

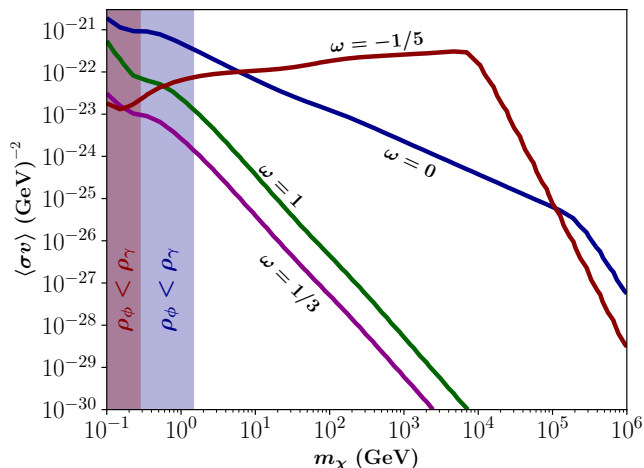


FIG. 18. Parameter space $(m_\chi, \langle\sigma v\rangle)$ for the FIMP DM candidate with $T_{\text{end}} = 7 \times 10^{-3}$ GeV and $\hat{\xi}_0 = 10^{-2}$. The solid red, blue, green, and magenta lines correspond to the parameter space that reproduces the current DM relic density for $\omega = -1/5, 0, 1,$ and $1/3$, respectively. The blue and red zones represent the parameter space in which $\rho_\phi < \rho_\gamma, \forall t$, for $\omega = 0$ and $-1/5$, respectively. For illustrative purposes, the curves corresponding to $\omega = -1/5$ and $\omega = 0$ were obtained with $\kappa = 10^{-3}$, while the curve for $\omega = 1/3$ was obtained using $\kappa = 1$, and the curve for $\omega = 1$ with $\kappa = 10^3$.

accurately reproduce the current DM relic density by adjusting both, the model and DM parameters within this novel NSC framework for FIMP DM candidates.

The main finding of our work is that the inclusion of bulk viscosity in NSCs brings to light DM parameters that are disregarded in both, Λ CDM and the classical NSC scenarios, as it was shown in Figure 7, giving us new windows to search for FIMP DM candidates. In

particular, modifying the values of m_χ and $\langle\sigma v\rangle$ can shift the parameters (T_{end}, κ) that reproduce the current DM relic density. For example, an increment in the values of m_χ and $\langle\sigma v\rangle$ can shift the parameter space upward to the right (Figure 12) and upward to the left (Figure 13), respectively. These displacements can be combined to reach new windows of allowed parameters if a signal of DM is experimentally detected. In the same line, larger values of $\hat{\xi}_0$ (Figure 14) make more prominent the curvature to the approximately independent κ zone (as it was described in Section III A) and shift the parameters downward to the right. On the other hand, modifying the model parameters shifts the $(m_\chi, \langle\sigma v\rangle)$ values that reproduce the current DM relic density. In particular, increasing the values of κ and T_{end} shift the parameter space upward (Figure 15) and downward to the right (Figure 16), respectively, reaching larger values of $\langle\sigma v\rangle$ and m_χ . In this sense, larger values of $\hat{\xi}_0$ (Figure 17) make significant imprints in the DM parameters reaching larger values of $\langle\sigma v\rangle$.

Therefore, this paper is a further step in the study of FIMPs as DM candidates and a first approximation to highlight the imprints that the bulk viscosity can leave in these particles and their relic density in the early universe through a NSC scenario. In this sense, this work, in collaboration with Ref. [118], provides a comprehensive set of possibilities for opening new avenues of research in the study of FIMPs and WIMPs as DM candidates.

ACKNOWLEDGMENTS

E.G. acknowledges the scientific support of Núcleo de Investigación No. 7 UCN-VRIDT 076/2020, Núcleo de Modelación y Simulación Científica (NMSC).

-
- [1] A. G. Riess *et al.* (Supernova Search Team), *Astron. J.* **116**, 1009 (1998), [arXiv:astro-ph/9805201](#).
 - [2] S. Perlmutter *et al.* (Supernova Cosmology Project), *Astrophys. J.* **517**, 565 (1999), [arXiv:astro-ph/9812133](#).
 - [3] D. Scolnic *et al.*, *Astrophys. J.* **938**, 113 (2022), [arXiv:2112.03863 \[astro-ph.CO\]](#).
 - [4] M. Moresco *et al.*, *JCAP* **08**, 006, [arXiv:1201.3609 \[astro-ph.CO\]](#).
 - [5] C. Zhang, H. Zhang, S. Yuan, T.-J. Zhang, and Y.-C. Sun, *Res. Astron. Astrophys.* **14**, 1221 (2014), [arXiv:1207.4541 \[astro-ph.CO\]](#).
 - [6] M. Moresco, *Mon. Not. Roy. Astron. Soc.* **450**, L16 (2015), [arXiv:1503.01116 \[astro-ph.CO\]](#).
 - [7] D. J. Eisenstein *et al.* (SDSS), *Astrophys. J.* **633**, 560 (2005), [arXiv:astro-ph/0501171](#).
 - [8] C. L. Bennett *et al.* (WMAP), *Astrophys. J. Suppl.* **208**, 20 (2013), [arXiv:1212.5225 \[astro-ph.CO\]](#).
 - [9] N. Aghanim *et al.* (Planck), *Astron. Astrophys.* **641**, A6 (2020), [Erratum: *Astron. Astrophys.* 652, C4 (2021)], [arXiv:1807.06209 \[astro-ph.CO\]](#).
 - [10] G. Jungman, M. Kamionkowski, and K. Griest, *Phys. Rept.* **267**, 195 (1996), [arXiv:hep-ph/9506380](#).
 - [11] S. F. King and J. P. Roberts, *JHEP* **01**, 024, [arXiv:hep-ph/0608135](#).
 - [12] P. Arias, D. Cadamuro, M. Goodsell, J. Jaeckel, J. Redondo, and A. Ringwald, *JCAP* **06**, 013, [arXiv:1201.5902 \[hep-ph\]](#).
 - [13] A. Ringwald, *Phys. Dark Univ.* **1**, 116 (2012), [arXiv:1210.5081 \[hep-ph\]](#).
 - [14] G. Steigman and M. S. Turner, *Nucl. Phys. B* **253**, 375 (1985).
 - [15] G. Bertone, D. Hooper, and J. Silk, *Phys. Rept.* **405**, 279 (2005), [arXiv:hep-ph/0404175](#).
 - [16] G. Arcadi, M. Dutra, P. Ghosh, M. Lindner, Y. Mambrini, M. Pierre, S. Profumo, and F. S. Queiroz, *Eur. Phys. J. C* **78**, 203 (2018), [arXiv:1703.07364 \[hep-ph\]](#).
 - [17] L. Roszkowski, E. M. Sessolo, and S. Trojanowski, *Rept. Prog. Phys.* **81**, 066201 (2018), [arXiv:1707.06277 \[hep-ph\]](#).

- [18] G. Arcadi, D. Cabo-Almeida, M. Dutra, P. Ghosh, M. Lindner, Y. Mambrini, J. P. Neto, M. Pierre, S. Profumo, and F. S. Queiroz, The Waning of the WIMP: Endgame? (2024), [arXiv:2403.15860 \[hep-ph\]](#).
- [19] N. Bernal, M. Heikinheimo, T. Tenkanen, K. Tuominen, and V. Vaskonen, *Int. J. Mod. Phys. A* **32**, 1730023 (2017), [arXiv:1706.07442 \[hep-ph\]](#).
- [20] X. Chu, T. Hambye, and M. H. G. Tytgat, *JCAP* **05**, 034, [arXiv:1112.0493 \[hep-ph\]](#).
- [21] L. J. Hall, K. Jedamzik, J. March-Russell, and S. M. West, *JHEP* **03**, 080, [arXiv:0911.1120 \[hep-ph\]](#).
- [22] G. Steigman, B. Dasgupta, and J. F. Beacom, *Phys. Rev. D* **86**, 023506 (2012), [arXiv:1204.3622 \[hep-ph\]](#).
- [23] G. F. Giudice, E. W. Kolb, and A. Riotto, *Phys. Rev. D* **64**, 023508 (2001), [arXiv:hep-ph/0005123](#).
- [24] P. Salati, *Phys. Lett. B* **571**, 121 (2003), [arXiv:astro-ph/0207396](#).
- [25] C. Pallis, *Astropart. Phys.* **21**, 689 (2004), [arXiv:hep-ph/0402033](#).
- [26] G. B. Gelmini and P. Gondolo, *Phys. Rev. D* **74**, 023510 (2006), [arXiv:hep-ph/0602230](#).
- [27] G. Gelmini, P. Gondolo, A. Soldatenko, and C. E. Yaguna, *Phys. Rev. D* **74**, 083514 (2006), [arXiv:hep-ph/0605016](#).
- [28] L. Randall, J. Scholtz, and J. Unwin, *JHEP* **03**, 011, [arXiv:1509.08477 \[hep-ph\]](#).
- [29] T. Tenkanen and V. Vaskonen, *Phys. Rev. D* **94**, 083516 (2016), [arXiv:1606.00192 \[astro-ph.CO\]](#).
- [30] S. Hamdan and J. Unwin, *Mod. Phys. Lett. A* **33**, 1850181 (2018), [arXiv:1710.03758 \[hep-ph\]](#).
- [31] F. D’Eramo, N. Fernandez, and S. Profumo, *JCAP* **02**, 046, [arXiv:1712.07453 \[hep-ph\]](#).
- [32] F. D’Eramo, N. Fernandez, and S. Profumo, *JCAP* **05**, 012, [arXiv:1703.04793 \[hep-ph\]](#).
- [33] L. Visinelli, *Symmetry* **10**, 546 (2018), [arXiv:1710.11006 \[astro-ph.CO\]](#).
- [34] M. Drees and F. Hajkarim, *JHEP* **12**, 042, [arXiv:1808.05706 \[hep-ph\]](#).
- [35] N. Bernal, C. Cosme, and T. Tenkanen, *Eur. Phys. J. C* **79**, 99 (2019), [arXiv:1803.08064 \[hep-ph\]](#).
- [36] N. Bernal, C. Cosme, T. Tenkanen, and V. Vaskonen, *Eur. Phys. J. C* **79**, 30 (2019), [arXiv:1806.11122 \[hep-ph\]](#).
- [37] A. Poulin, *Phys. Rev. D* **100**, 043022 (2019), [arXiv:1905.03126 \[hep-ph\]](#).
- [38] C. Maldonado and J. Unwin, *JCAP* **06**, 037, [arXiv:1902.10746 \[hep-ph\]](#).
- [39] P. Arias, N. Bernal, A. Herrera, and C. Maldonado, *JCAP* **10**, 047, [arXiv:1906.04183 \[hep-ph\]](#).
- [40] N. Bernal, F. Elahi, C. Maldonado, and J. Unwin, *JCAP* **11**, 026, [arXiv:1909.07992 \[hep-ph\]](#).
- [41] C. Cosme, M. Dutra, T. Ma, Y. Wu, and L. Yang, *JHEP* **03**, 026, [arXiv:2003.01723 \[hep-ph\]](#).
- [42] G. Arcadi, J. P. Neto, F. S. Queiroz, and C. Siqueira, *Phys. Rev. D* **105**, 035016 (2022), [arXiv:2108.11398 \[hep-ph\]](#).
- [43] P. Arias, N. Bernal, D. Karamitros, C. Maldonado, L. Roszkowski, and M. Venegas, *JCAP* **11**, 003, [arXiv:2107.13588 \[hep-ph\]](#).
- [44] N. Bernal and Y. Xu, *JCAP* **12**, 017, [arXiv:2209.07546 \[hep-ph\]](#).
- [45] M. R. Haque, D. Maity, and R. Mondal, *JHEP* **09**, 012, [arXiv:2301.01641 \[hep-ph\]](#).
- [46] J. Silva-Malpartida, N. Bernal, J. Jones-Pérez, and R. A. Lineros, *JCAP* **09**, 015, [arXiv:2306.14943 \[hep-ph\]](#).
- [47] B. Barman, N. Bernal, and Y. Xu, *JCAP* **08**, 014, [arXiv:2404.16090 \[hep-ph\]](#).
- [48] D. K. Ghosh, A. Ghoshal, and S. Jeusun, *JHEP* **01**, 026, [arXiv:2305.09188 \[hep-ph\]](#).
- [49] J. Silva-Malpartida, N. Bernal, J. Jones-Pérez, and R. A. Lineros, From WIMPs to FIMPs: Impact of Early Matter Domination (2024), [arXiv:2408.08950 \[hep-ph\]](#).
- [50] G. Arcadi, M. Lindner, J. P. Neto, and F. S. Queiroz, Ultraheavy Dark Matter and WIMPs Production aided by Primordial Black Holes (2024), [arXiv:2408.13313 \[hep-ph\]](#).
- [51] C. Maldonado and F. Mendez, *Phys. Rev. D* **103**, 123505 (2021), [arXiv:2103.11235 \[gr-qc\]](#).
- [52] C. Maldonado and F. Mendez, *Int. J. Mod. Phys. D* **32**, 2350059 (2023), [arXiv:2304.00620 \[hep-ph\]](#).
- [53] C. Maldonado and F. Méndez, *Universe* **9**, 429 (2023).
- [54] R. Maartens (1996) [arXiv:astro-ph/9609119](#).
- [55] C. Eckart, *Phys. Rev.* **58**, 267 (1940).
- [56] C. Eckart, *Phys. Rev.* **58**, 919 (1940).
- [57] J. M. Stewart, *Proc. R. Soc. A* **357**, 59 (1977).
- [58] W. Israel and J. M. Stewart, *Proc. R. Soc. A* **365**, 43 (1979).
- [59] W. Israel, *Annals Phys.* **100**, 310 (1976).
- [60] R. Maartens, *Class. Quant. Grav.* **12**, 1455 (1995).
- [61] S. Floerchinger, N. Tetradis, and U. A. Wiedemann, *Phys. Rev. Lett.* **114**, 091301 (2015), [arXiv:1411.3280 \[gr-qc\]](#).
- [62] W. Zimdahl, *Mon. Not. Roy. Astron. Soc.* **280**, 1239 (1996), [arXiv:astro-ph/9602128](#).
- [63] J. R. Wilson, G. J. Mathews, and G. M. Fuller, *Phys. Rev. D* **75**, 043521 (2007), [arXiv:astro-ph/0609687](#).
- [64] G. J. Mathews, N. Q. Lan, and C. Kolda, *Phys. Rev. D* **78**, 043525 (2008), [arXiv:0801.0853 \[astro-ph\]](#).
- [65] S. Hofmann, D. J. Schwarz, and H. Stoecker, *Phys. Rev. D* **64**, 083507 (2001), [arXiv:astro-ph/0104173](#).
- [66] R. Foot and S. Vagnozzi, *Phys. Rev. D* **91**, 023512 (2015), [arXiv:1409.7174 \[hep-ph\]](#).
- [67] R. Foot and S. Vagnozzi, *JCAP* **07**, 013, [arXiv:1602.02467 \[astro-ph.CO\]](#).
- [68] D. Blas, S. Floerchinger, M. Garny, N. Tetradis, and U. A. Wiedemann, *JCAP* **11**, 049, [arXiv:1507.06665 \[astro-ph.CO\]](#).
- [69] G. Goswami, G. K. Chakravarty, S. Mohanty, and A. R. Prasanna, *Phys. Rev. D* **95**, 103509 (2017), [arXiv:1603.02635 \[hep-ph\]](#).
- [70] M. G. Alford, L. Bovard, M. Hanauske, L. Rezzolla, and K. Schwenzer, *Phys. Rev. Lett.* **120**, 041101 (2018), [arXiv:1707.09475 \[gr-qc\]](#).
- [71] S. Nojiri and S. D. Odintsov, *Phys. Rev. D* **70**, 103522 (2004), [arXiv:hep-th/0408170](#).
- [72] S. Capozziello, V. F. Cardone, E. Elizalde, S. Nojiri, and S. D. Odintsov, *Phys. Rev. D* **73**, 043512 (2006), [arXiv:astro-ph/0508350](#).
- [73] S. Nojiri and S. D. Odintsov, *Phys. Rev. D* **72**, 023003 (2005), [arXiv:hep-th/0505215](#).
- [74] M. Cataldo, N. Cruz, and S. Lepe, *Phys. Lett. B* **619**, 5 (2005), [arXiv:hep-th/0506153](#).
- [75] I. H. Brevik, *Gen. Rel. Grav.* **38**, 1317 (2006), [arXiv:gr-qc/0603025](#).
- [76] N. Cruz, S. Lepe, and F. Peña, *Phys. Lett. B* **767**, 103 (2017), [arXiv:1607.04192 \[gr-qc\]](#).

- [77] H. Velten and D. Schwarz, *Phys. Rev. D* **86**, 083501 (2012), arXiv:1206.0986 [astro-ph.CO].
- [78] G. Acquaviva and A. Beesham, *Phys. Rev. D* **90**, 023503 (2014), arXiv:1405.3459 [gr-qc].
- [79] M. Cruz, N. Cruz, and S. Lepe, *Phys. Rev. D* **96**, 124020 (2017), arXiv:1710.02607 [gr-qc].
- [80] N. Cruz, E. González, S. Lepe, and D. Sáez-Chillón Gómez, *JCAP* **12**, 017, arXiv:1807.10729 [gr-qc].
- [81] N. Cruz, E. González, and J. Jovel, *Symmetry* **14**, 1866 (2022), arXiv:2202.02362 [gr-qc].
- [82] N. Cruz, E. González, and J. Jovel, *Mod. Phys. Lett. A* **38**, 2350088 (2023), arXiv:2207.14244 [gr-qc].
- [83] G. Gómez, G. Palma, E. González, A. Rincón, and N. Cruz, *Eur. Phys. J. Plus* **138**, 738 (2023), arXiv:2210.09429 [gr-qc].
- [84] N. Cruz, G. Gomez, E. González, G. Palma, and A. Rincon, *Phys. Dark Univ.* **42**, 101351 (2023), arXiv:2304.12407 [gr-qc].
- [85] J. C. Fabris, S. V. B. Goncalves, and R. de Sa Ribeiro, *Gen. Rel. Grav.* **38**, 495 (2006), arXiv:astro-ph/0503362.
- [86] A. Avelino and U. Nucamendi, *JCAP* **04**, 006, arXiv:0811.3253 [gr-qc].
- [87] B. Li and J. D. Barrow, *Phys. Rev. D* **79**, 103521 (2009), arXiv:0902.3163 [gr-qc].
- [88] A. Avelino and U. Nucamendi, *JCAP* **08**, 009, arXiv:1002.3605 [gr-qc].
- [89] W. S. Hipolito-Ricaldi, H. E. S. Velten, and W. Zimdahl, *Phys. Rev. D* **82**, 063507 (2010), arXiv:1007.0675 [astro-ph.CO].
- [90] H. Velten and D. J. Schwarz, *JCAP* **09**, 016, arXiv:1107.1143 [astro-ph.CO].
- [91] J.-S. Gagnon and J. Lesgourgues, *JCAP* **09**, 026, arXiv:1107.1503 [astro-ph.CO].
- [92] M. Bruni, R. Lazkoz, and A. Rozas-Fernandez, *Mon. Not. Roy. Astron. Soc.* **431**, 2907 (2013), arXiv:1210.1880 [astro-ph.CO].
- [93] M. Cruz, N. Cruz, and S. Lepe, *Phys. Lett. B* **769**, 159 (2017), arXiv:1701.06724 [gr-qc].
- [94] N. Cruz, E. González, and G. Palma, *Gen. Rel. Grav.* **52**, 62 (2020), arXiv:1812.05009 [gr-qc].
- [95] N. Cruz, E. González, and G. Palma, *Mod. Phys. Lett. A* **36**, 2150032 (2021), arXiv:1906.04570 [gr-qc].
- [96] M. K. Mak and T. Harko, *Int. J. Mod. Phys. D* **13**, 273 (2004), arXiv:gr-qc/0311050.
- [97] T. Padmanabhan and S. M. Chitre, *Phys. Lett. A* **120**, 433 (1987).
- [98] J. D. Barrow, *Nucl. Phys. B* **310**, 743 (1988).
- [99] R. Maartens and V. Mendez, *Phys. Rev. D* **55**, 1937 (1997), arXiv:astro-ph/9611205.
- [100] A. Avelino, Y. Leyva, and L. A. Urena-Lopez, *Phys. Rev. D* **88**, 123004 (2013), arXiv:1306.3270 [astro-ph.CO].
- [101] A. Hernández-Almada, M. A. García-Aspeitia, J. Magaña, and V. Motta, *Phys. Rev. D* **101**, 063516 (2020), arXiv:2001.08667 [astro-ph.CO].
- [102] I. H. Brevik, O. Gorbunova, and Y. A. Shaïdo, *Int. J. Mod. Phys. D* **14**, 1899 (2005), arXiv:gr-qc/0508038.
- [103] I. H. Brevik and O. Gorbunova, *Gen. Rel. Grav.* **37**, 2039 (2005), arXiv:gr-qc/0504001.
- [104] I. H. Brevik and O. Gorbunova, *Eur. Phys. J. C* **56**, 425 (2008), arXiv:0806.1399 [gr-qc].
- [105] I. Brevik, O. Gorbunova, and D. Saez-Gomez, *Gen. Rel. Grav.* **42**, 1513 (2010), arXiv:0908.2882 [gr-qc].
- [106] I. Brevik, S. Nojiri, S. D. Odintsov, and D. Saez-Gomez, *Eur. Phys. J. C* **69**, 563 (2010), arXiv:1002.1942 [hep-th].
- [107] I. Brevik, E. Elizalde, S. Nojiri, and S. D. Odintsov, *Phys. Rev. D* **84**, 103508 (2011), arXiv:1107.4642 [hep-th].
- [108] F. Contreras, N. Cruz, and E. González, *J. Phys. Conf. Ser.* **720**, 012014 (2016), arXiv:1510.02782 [gr-qc].
- [109] F. Contreras, N. Cruz, E. Elizalde, E. González, and S. Odintsov, *Phys. Rev. D* **98**, 123520 (2018), arXiv:1808.06546 [gr-qc].
- [110] N. Cruz, E. González, and J. Jovel, *Phys. Rev. D* **105**, 024047 (2022), arXiv:2109.09865 [gr-qc].
- [111] D. Barta, *Class. Quant. Grav.* **36**, 215012 (2019), arXiv:1904.00907 [gr-qc].
- [112] S. Bravo Medina, M. Nowakowski, and D. Batic, *Class. Quant. Grav.* **36**, 215002 (2019), arXiv:1901.09787 [gr-qc].
- [113] K. L. Pandey, T. Karwal, and S. Das, *JCAP* **07**, 026, arXiv:1902.10636 [astro-ph.CO].
- [114] W. Yang, S. Pan, E. Di Valentino, A. Paliathanasis, and J. Lu, *Phys. Rev. D* **100**, 103518 (2019), arXiv:1906.04162 [astro-ph.CO].
- [115] E. Di Valentino, O. Mena, S. Pan, L. Visinelli, W. Yang, A. Melchiorri, D. F. Mota, A. G. Riess, and J. Silk, *Class. Quant. Grav.* **38**, 153001 (2021), arXiv:2103.01183 [astro-ph.CO].
- [116] B. D. Normann and I. H. Brevik, *Mod. Phys. Lett. A* **36**, 2150198 (2021), arXiv:2107.13533 [gr-qc].
- [117] I. Brevik, O. Grøn, J. de Haro, S. D. Odintsov, and E. N. Saridakis, *Int. J. Mod. Phys. D* **26**, 1730024 (2017), arXiv:1706.02543 [gr-qc].
- [118] E. González, C. Maldonado, N. S. Mite, and R. Salinas, *JCAP* **10**, 088, arXiv:2409.03083 [hep-ph].
- [119] L. Kofman, A. D. Linde, and A. A. Starobinsky, *Phys. Rev. D* **56**, 3258 (1997), arXiv:hep-ph/9704452.
- [120] L. Ackerman, W. Fischler, S. Kundu, and N. Sivanandam, *JCAP* **05**, 024, arXiv:1007.3511 [astro-ph.CO].
- [121] M. A. G. Garcia, K. Kaneta, Y. Mambrini, and K. A. Olive, *Phys. Rev. D* **101**, 123507 (2020), arXiv:2004.08404 [hep-ph].
- [122] M. A. G. Garcia, K. Kaneta, Y. Mambrini, and K. A. Olive, *JCAP* **04**, 012, arXiv:2012.10756 [hep-ph].
- [123] M. R. Haque, D. Maity, and R. Mondal, Thermal and non-thermal dark matters with gravitational neutrino reheating (2024), arXiv:2408.12450 [hep-ph].
- [124] S. Sarkar, *Rept. Prog. Phys.* **59**, 1493 (1996), arXiv:hep-ph/9602260.
- [125] S. Hannestad, *Phys. Rev. D* **70**, 043506 (2004), arXiv:astro-ph/0403291.
- [126] F. De Bernardis, L. Pagano, and A. Melchiorri, *Astropart. Phys.* **30**, 192 (2008).
- [127] S. Weinberg and R. H. Dicke, *Gravitation and Cosmology: Principles and Applications of the General Theory of Relativity*, edited by Wiley.
- [128] D. Chowdhury and A. Hait, *JHEP* **09**, 085, arXiv:2302.06654 [hep-ph].